Two-Stage Sequentially Operated Regenerative Converters with Controlled Flywheeling

SUBBANNA P. BHAT AND GOPAL K. DUBEY, SENIOR MEMBER, IEEE

Abstract—**Separately excited dc motors fed by sequentially operated multistage converters are commonly used in mainline traction. The drive performance can be greatly improved by operating the fully controlled converters with controlled flywheeling. The analysis and performance of dc drive fed by two-stage sequentially operated fully controlled converters with controlled flywheeling are described. The modes of operation of the converter system are identified, and a method of performance calculation, taking these modes of operation into account, is presented. The nomograms and the analytical method of calculating them are presented for the calculation of optimum value of filter inductance. The performance of the drive with controlled flywheeling is compared with that with normal control. The modes of operation and certain aspects of drive performance are verified experimentally.**

I. INTRODUCTION

TRACTION ac supplies are generally restricted to single phase at considerable power levels. In such applications, usually a separately excited dc motor is fed by a converter circuit. In order to improve the system performance, it is quite common to employ multistage converter circuits and operate them under sequence control technique [1].

The performance of single-phase converter systems can be greatly improved if a controlled flywheeling technique is employed in fully controlled converters [2], [3]. The output voltage waveform of a single-stage converter employing controlled flywheeling is similar to that of a two-stage sequentially operated fully controlled converter circuit. Therefore, controlled flywheeling in a two-stage converter circuit improves the system performance to a level which can otherwise be obtained by a four-stage fully controlled converter circuit [4].

In this paper, the analysis and performance of a two-stage converter circuit employing controlled flywheeling and feeding a dc separately excited motor are presented. Various modes of system operation are identified, and the drive is analyzed taking these modes into account. A method is described for choosing an optimum value of filter inductance. Nomograms are presented for the controlled flywheeling and the normal control techniques, from which a filter inductance can be chosen for any dc separately excited motor. The various parameters of the system performance with controlled flywheeling are compared with those of normal control technique for the same developed power. The modes of operation and certain aspects of drive performance are verified experimentally.

Paper IPCSD 85-06 and 83-31, approved by the Static Power Converter Committee of the IEEE Industry Applications Society for publication in this TRANSACTIONS. Manuscript released for publication January 21, 1985.

S. P. Bhat is with the Department of Electrical Engineering, Karnataka Regional Engineering College, Dakshina Kannada District, Karnataka State, India.

G. K. Dubey was with the Department of Electrical Engineering, Virginia Polytechnic Institute, Blacksburg, VA 24061. He is now with the Department of Electrical Engineering, Indian Institute of Technology, Kanpur, 208016, India.

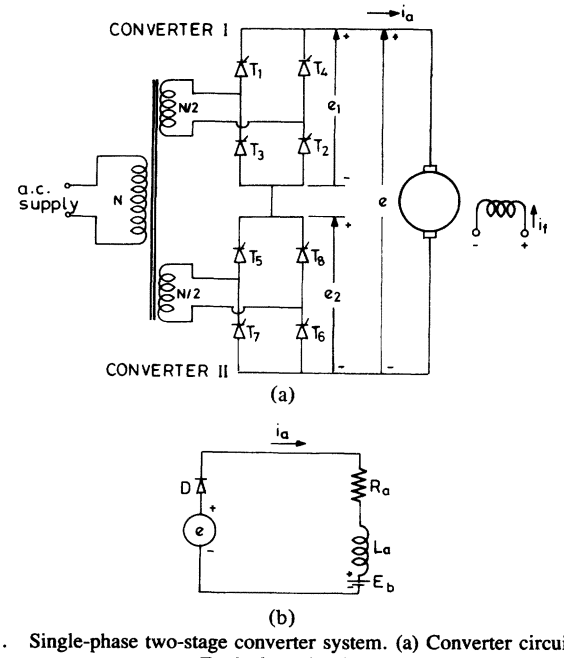

Fig. 1. Single-phase two-stage converter system. (a) Converter circuit. (b) Equivalent circuit.

II. MODES OF CONVERTER OPERATION

Fig. 1 shows a two-stage converter system and its equivalent circuit. The identification of modes of converter operation and the system analysis are done assuming that the thyristors are ideal switches and the source inductance is negligible. Both the secondaries of supply transformer have an equal number of turns.

So far as the output voltage magnitude is within half of its full range (i.e., $0.5 > E_{on} > -0.5$), only one of the converters remains active. (Symbols are defined in the Nomenclature at the end of the paper.) That is, the second converter does not feed any power to the load but allows the load current to flow through either pair of its series-aiding thyristors. When the per unit magnitude of output voltage is larger than half (i.e., $1.0 > |E_{on}| > 0.5$), both the converters become active. Therefore, the system operation is broadly divided into four categories depending upon the number of active converters and whether the system is under motoring or regenerating condition. These modes of system operation and

0093-9994/85/1100-1441$01.00

TABLE I

Mode of system operation	System condition	Output voltage range	Converters that are active	Firing/Flywheeling angles			
				α_{p1}	α_{p2}	α_{n1}	α_{n2}
I	motoring	$0<E_{on}<0.5$	I	variable	π	0	0
II	motoring	$0.5<E_{on}<1.0$	I, II	0	variable	0	0
III	regeneration	$0>E_{on}>-0.5$	I	π	π	variable	0
IV	regeneration	$-0.5>E_{on}>-1.0$	I, II	π	π	π	variable

TABLE II

Mode of Converter Operation	System Condition[a]	Mode of System Operation	Nature of Armature Current[b]	Relationship Between α, β, and γ	Refer to Figure
1	M	I	D	$\alpha_{p1}<\beta_{p1}<\gamma_{p1}$	2(a)
2	M	I	D	$\beta_{p1}<\alpha_{p1}<\gamma_{p1}$	2(b)
3	M	I	D	$\beta_{p1}<\gamma_{p1}<\alpha_{p1}$	2(c)
4	M	I	C	—	2(d)
5	M	II	D	$\alpha_{p2}<\beta_{p2}<\gamma_{p2}$	2(e)
6	M	II	D	$\beta_{p2}<\alpha_{p2}<\gamma_{p2}$	2(f)
7	M	II	D	$\beta_{p2}<\gamma_{p2}<\alpha_{p2}$	2(g)
8	M	II	D	$\gamma_{p1}<\beta_{p2}<a_{p2}<\beta_{p2}'$	2(h)
9	M	II	D	$\beta_{p2}<\gamma_{p1}<\alpha_{p2}$	2(i)
10	M	II	C	—	2(j)
11	R	III	D	$\beta_{n1}<\alpha_{n1}<\gamma_{n1}$	2(k)
12	R	III	D	$\beta_{n1}<\gamma_{n1}<\alpha_{n1}$	2(l)
13	R	III	C	—	2(m)
14	R	IV	D	$\beta_{n2}<\alpha_{n2}<\gamma_{n1}$	2(n)
15	R	IV	D	$\alpha_{n2}<\beta_{n2}<\gamma_{n1}$	2(o)
16	R	IV	D	$\beta_{n2}<\alpha_{n2}<\beta_{n2}'<\gamma_{n1}$	2(p)
17	R	IV	D	$\beta_{n2}<\alpha_{n2}$	2(q)
18	R	IV	D	$\beta_{n2}<\gamma_{n2}<\alpha_{n2}$	2(r)
19	R	IV	C	—	2(s)

[a] M = motoring, R = regenerating.
[b] D = discontinuous, C = continuous.

the corresponding firing/flywheeling angles of the converters are listed in Table I.

In the case of a dc motor load, if the armature current is discontinuous, the waveform of converter output voltage depends not only on the firing angle but also on the motor back EMF. When the load current is continuous, the voltage across the incoming thyristors is determined only by the supply voltage. Therefore, the incoming pair of thyristors can be triggered into conduction at any instant during the half-cycle. However, when the armature current is reduced to zero, the forward voltage across the thyristors is determined by the difference between the supply voltage and motor back EMF. This gives rise to modification of the waveform of converter output voltage. Depending upon the waveshape of the output voltage, the converter operation is classified into different modes of converter operation. A total of 19 such modes are identified, which are listed in Table II and Fig. 2. Among these, modes 1–4 and 11–13 occur when only converter I is active; therefore, these modes are similar to that of single-stage converter operation. A brief explanation of the various modes and their interrelationship are given in the following paragraphs.

Four modes of converter operation exist (modes 4, 9, 13, and 19) in which the armature current is continuous. However, these modes occur only when the motor back EMF is sufficiently low (or negative). When the motor is operating on light loads, a number of discontinuous current modes can occur depending upon the firing/flywheeling angle.

In the case of mode 1 (Fig. 2(a)), when thyristor T_1 is triggered at α_{p1}, the armature current is still nonzero, and therefore T_4 gets line-commuted. Since the instantaneous supply voltage is still smaller than the motor back EMF, it causes the armature current to reduce further and eventually become zero. Since the thyristors are supplied with extended gate pulses, T_1 (along with T_2, T_6, and T_8) regains conduction at γ_{p1}, when the supply voltage becomes greater than the motor back EMF.

In the case of mode 2, by the time T_1 is triggered, the armature current has already become zero, and the supply voltage is less than the motor back EMF. Therefore, T_1 starts conducting only at γ_{p1}. In the case of mode 3, at the instant of triggering of T_1, the supply voltage is larger than the motor back EMF. Therefore, conduction begins without any delay.

When the converter is operating in mode 1 or mode 3, if the motor back EMF is reduced, the converter operation changes into mode 4. In the case of mode 2, a decrease in the motor back EMF would eventually bring about the condition of either $\beta_{p1} = \alpha_{p1} < \gamma_{p1}$ or $\beta_{p1} < \alpha_{p1} = \gamma_{p1}$. In the former case, mode 2 changes over to mode 1 and, in the latter case, to mode 3. Another remote possibility is that, with the decrease in E_b,

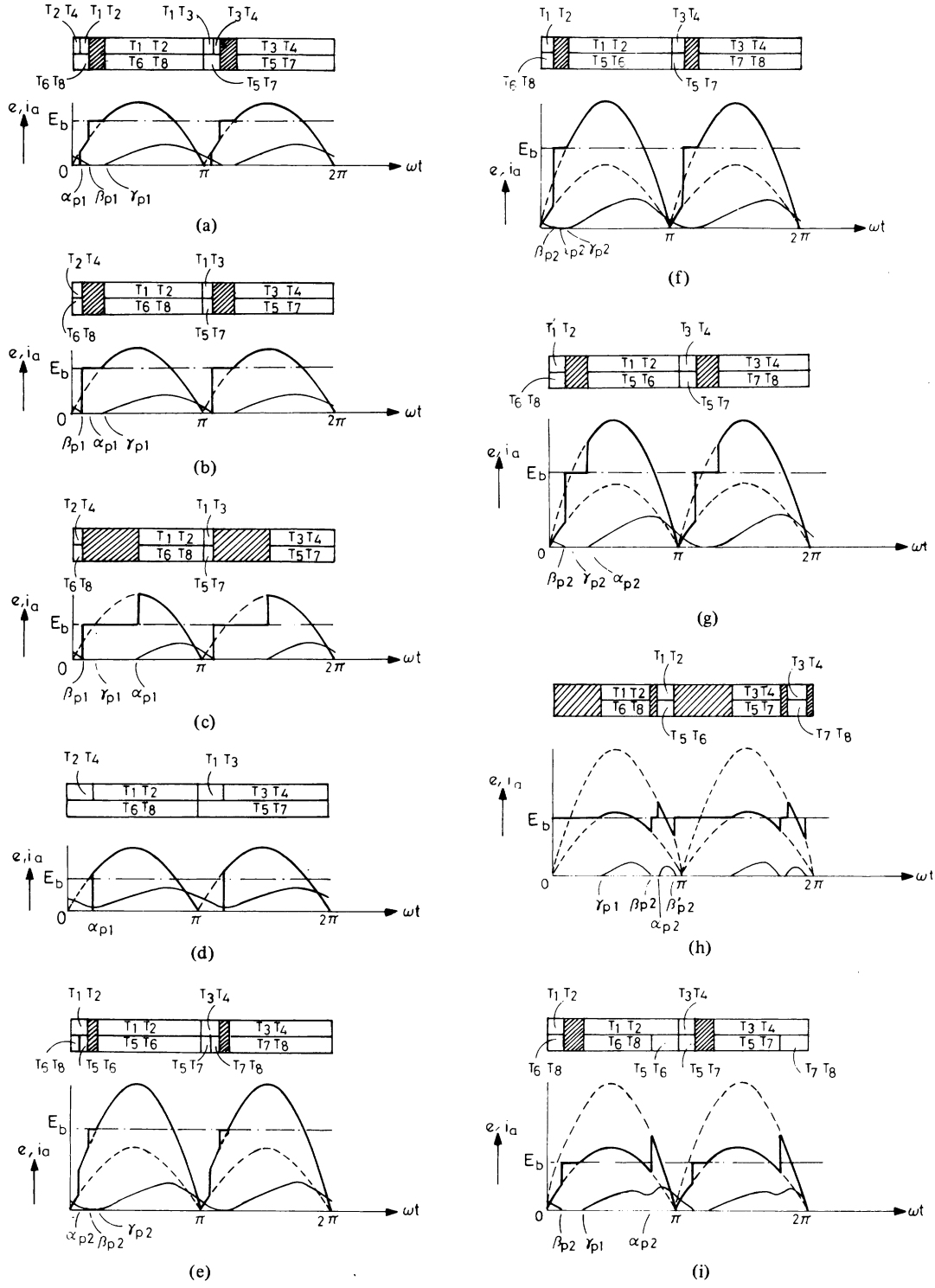

Fig. 2. Modes of converter operation. (a) Mode 1. (b) Mode 2. (c) Mode 3. (d) Mode 4. (e) Mode 5. (f) Mode 6. (g) Mode 7. (h) Mode 8. (i) Mode 9. (j) Mode 10. (k) Mode 11. (l) Mode 12. (m) Mode 13. (n) Mode 14. (o) Mode 15. (p) Mode 16. (q) Mode 17. (r) Mode 18. (s) Mode 19.

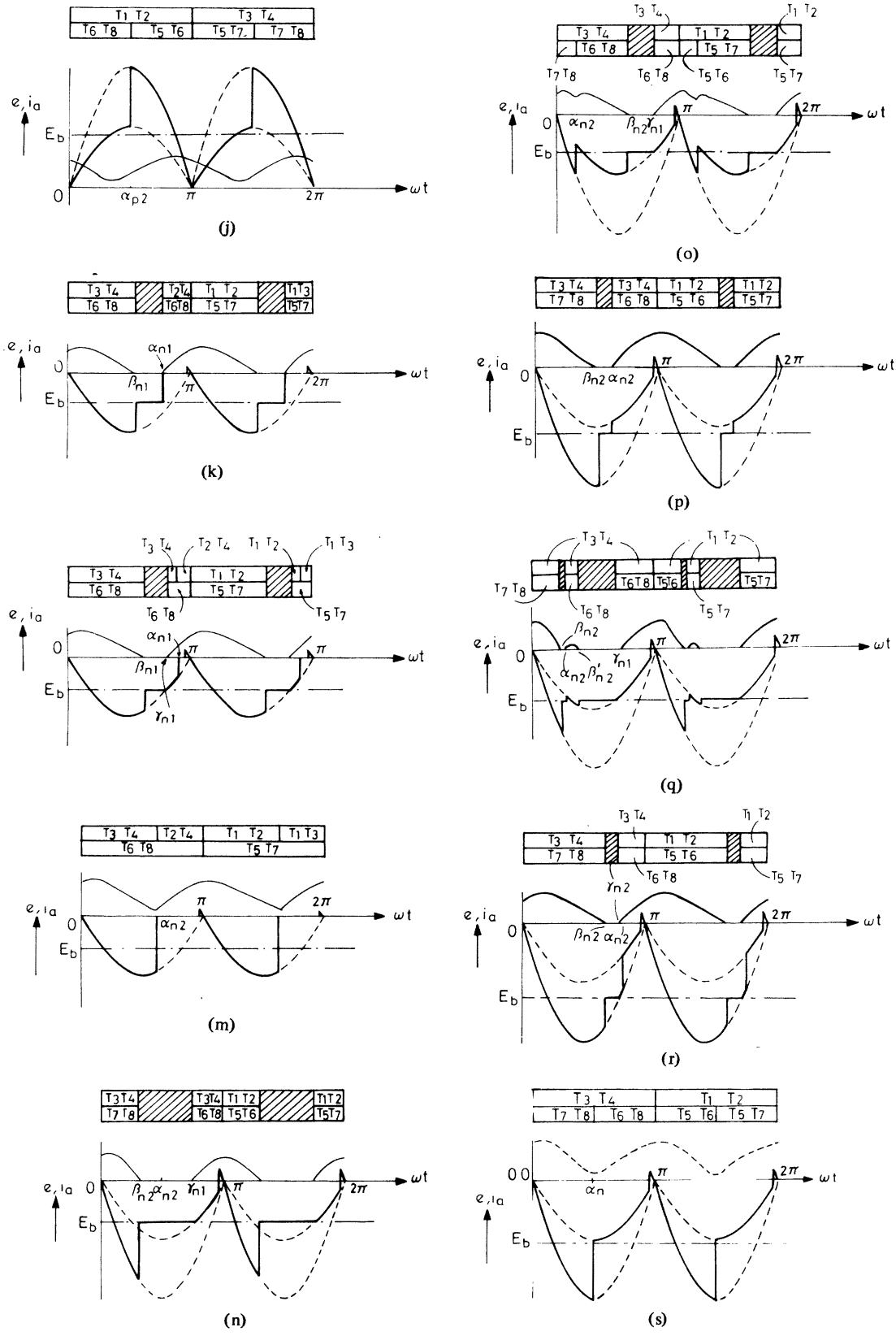

Fig. 2. (*Continued*)

both β_{p1} and γ_{p1} would touch α_{p1} simultaneously. In this case mode 2 directly changes over to mode 4.

A schematic representation of this interrelationship is shown in Fig. 3(a). The arrow in the diagram indicates the increase of armature current obtained by the reduction of motor back EMF.

When a discontinuous current mode touches a continuous current mode, the relative magnitude of X (angle at which the armature current is just zero) with respect to firing/flywheeling angle is also indicated in Fig. 3. This information is useful in the calculation of optimum filter inductance in the next section.

Modes 5–10 occur when both the converters supply power to the load. In this category (i.e., system operation mode II), converter I is maintained active all the time, and the output voltage variation (i.e., $1.0 > E_{on} > 0.5$) is obtained by varying the firing angle α_{p2}. Modes 5, 6, and 7 are similar to the modes 1, 2, and 3, respectively. In the case of mode 8, armature current becomes discontinuous twice during a half cycle. The possibility of this mode occurring in a practical circuit is remote, since it requires the armature circuit time constant to be very small. However, a slight decrease in the motor back EMF converts it into mode 9. The interrelationship between the various modes of this group (system operation mode II) is shown in Fig. 3(b).

In the case of modes 11–13, only one converter is active, and the system is regenerating (system operation mode III). In mode 11, the armature current becomes discontinuous at β_{n1}, and at α_{n1} the load begins to flywheel. During the interval β_{n1}–α_{n1}, no thyristor conducts; therefore, the converter terminal voltage is equal to the generated EMF of the motor. In the case of mode 12, the thyristors which have stopped conducting at β_{n1} regain conduction at γ_{n1} when the instantaneous supply voltage becomes more positive than the generated EMF E_b, and at α_{n1} the load begins to flywheel. Any increase in the generated EMF would cause this mode to change over to mode 13, but as far as mode 11 is concerned, depending upon the magnitude of α_{n1}, it may either directly change over to mode 13 or it may first convert itself to mode 12 and then finally to mode 13. In the former case (i.e., mode 11 directly changing over to mode 13), the minimum of armature current occurs at α_{n1}, and in the latter case it occurs at γ_{n1}. The interrelationship between the modes and the relative magnitude of X with respect to α_{n1} are shown in Fig. 3(c).

Modes 14–19 belong to the last group (system operation mode IV), in which converter I remains active all the time, and the output voltage variation (i.e., $-0.5 > E_{on} > -1.0$) is obtained by controlling the angle α_{n2}, at which converter II allows its load current to bypass its source. Except for this difference, mode 17 is similar to mode 11. In the case of both modes 14 and 15, after the load current has become zero, the thyristors regain conduction at γ_{n1}, when the supply voltage of converter I becomes more positive than the generated EMF; the difference between the two modes is caused by the relative magnitudes of β_{n2} and α_{n2}. In the case of mode 16, the current becomes discontinuous twice during a half cycle, but as in the case of mode 8, it rarely occurs in a practical circuit, since it requires the armature circuit time constant to be very small.

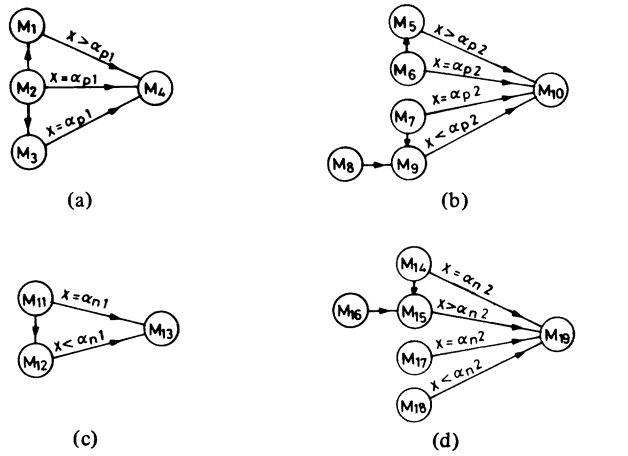

Fig. 3. Flowchart of modes of converter operation. (a) System mode I. (b) System mode II. (c) System mode III. (d) System mode IV. Arrow indicates increase in I_a.

Even otherwise, a slight increase in the generated EMF converts this mode into mode 15. In the case of mode 18, the period of discontinuity ends at γ_{n2} when both the converters are still active.

In the case of individual mode 15, 17, and 18, an increase of E_b in the negative direction would convert them to mode 19. However, in the case of mode 14, depending upon the flywheeling angle α_{n2}, it would either convert itself to mode 19 or to mode 15. The relationship between the modes is diagrammatically shown in Fig. 3(d).

Oscillograms of 16 out of the 19 modes (except modes 8, 16, and 18) are given in Fig. 4. These oscillograms are obtained for a 2.2 kW dc motor (Table III) load.

III. Choice of Optimum Value of Filter Inductance

Armature current ripple is an important factor in dc drives since it adversely affects the machine commutation and causes derating of the motor. If the armature current becomes discontinuous, the motor speed regulation deteriorates, and the sparking at the commutator brushes becomes more pronounced. Therefore, usually a filter inductance is incorporated in the armature circuit to limit the current ripple. On the other hand, the filter inductance cannot be made too large because of its cost, size, and weight considerations. This restriction becomes stringent in traction applications as the whole drive has to be accommodated in a relatively small space. The inevitable copper loss in the filter inductance, though small, is another factor which cannot be ignored. Therefore, it is useful to identify an optimum value of filter inductance required to eliminate discontinuous armature conduction and to maintain the current ripple within the specified permissible limis.

Dubey [5] has suggested a method of choosing an optimum value of filter inductance for chopper-fed dc drives. This technique is extended here for two-stage sequentially operated converter system. From the equivalent circuit of Fig. 1(b), the equation governing the system performance can be written as

$$e = L_a \frac{di_a}{dt} + R_a i_a + E_b. \tag{1}$$

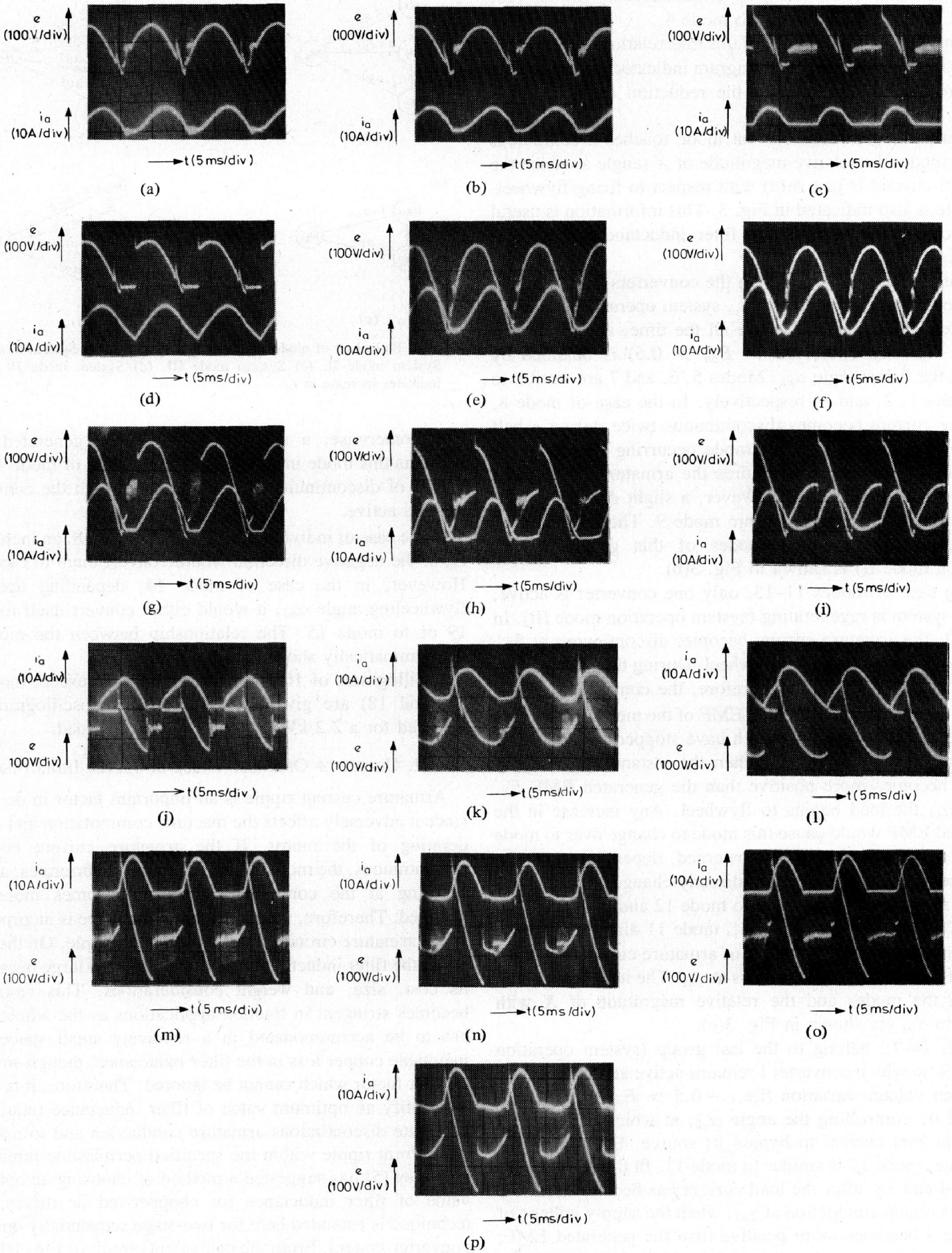

Fig. 4. Oscillograms of modes of converter operation. (a) Mode 1. (b) Mode 2. (c) Mode 3. (d) Mode 4. (e) Mode 5. (f) Mode 6. (g) Mode 7. (h) Mode 9. (i) Mode 10. (j) Mode 11. (k) Mode 12. (l) Mode 13. (m) Mode 14. (n) Mode 15. (o) Mode 17. (p) Mode 19.

TABLE III
DC MOTOR SPECIFICATIONS

Output power	2.2 kW
Armature voltage	220 V
Shunt field excitation	220 V
Current rating	11.6 A
Rated speed	1500 r/min
Armature resistance	2.0 Ω
Armature inductance	32.5 mH

In order to generalize the analysis, the voltages and currents of the system are normalized against the following base values:

$$\text{base voltage} = \frac{2E_m}{\pi}\ ;\ \text{base current} = \frac{2E_m}{\pi R_a}.$$

Thus the normalized performance equation of the system is given by

$$e_n = \tan\ \psi\ \frac{di_{an}}{dwt} + i_{an} + E_{bn}. \tag{2}$$

To select an optimum value of filter inductance, it is necessary to obtain the following curves for a set of values of armature circuit time constant:

1) normalized maximum armature current ripple (MCR) for the entire range of output voltage variation;
2) normalized boundary curve separating the regions of continuous and discontinuous armature conduction, in the speed–torque plane.

An analytic approach to obtain these curves is described in the following section. A computer flowchart is given in Fig. 5(a).

A. Calculation of MCR

For a particular firing angle, so far as the armature current is discontinuous, the current ripple depends upon the motor back EMF. When the armature current is continuous, any change in the motor back EMF causes change only in the dc component of armature current, and therefore the ripple is independent of motor back EMF. Thus, for a particular firing angle, the armature current ripple becomes maximum and remains constant when the current is continuous.

MCR can be analytically calculated by obtaining the current ripple for the continuous current modes of converter operation. An expression for armature current is obtained by solving (2), from which the expression for current slope can be derived. The instants at which the minimum and maximum of i_{an} occur (i.e., angles X and Y) can be determined by solving the expression for current slope. The MCR is then calculated with the help of the following expression:

$$\text{MCR} = \frac{i_{an}(Y) - i_{an}(X)}{2}. \tag{3}$$

Four modes of converter operation exist (modes 4, 10, 13, and 19) in which the armature current is continuous. The expressions for armature current for the various continuous current modes are given. Expressions for slopes can be obtained by differentiating these expressions.

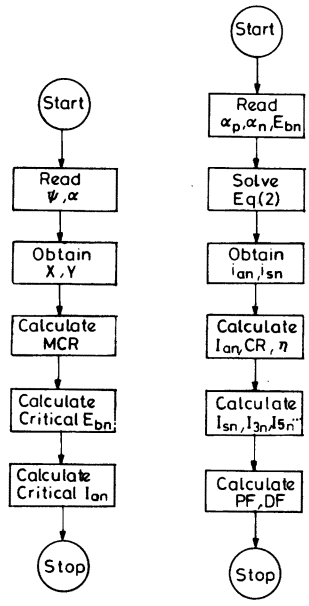

Fig. 5. Flowchart for system analysis.

Mode 4: In the interval $0 < wt < \alpha_{p1}$,

$$i_{an} = 0.5\ \cos\ \psi[[\sin\ \psi - \sin\ (\alpha_{p1} - \psi) \cdot \exp\ \{-(\pi - \alpha_{p1})\ \cot\ \psi\}] \cdot \exp\ (-wt\ \cot\ \psi) \div [1 - \exp\ (-\pi\ \cot\ \psi)]] - E_{bn} \tag{4}$$

and for the interval $\alpha_{p1} < wt < \pi$,

$$i_{an} = 0.5\ \cos\ \psi[\sin\ (wt - \psi) + [\sin\ \psi\ \exp\ (-\alpha_{p1}\ \cot\ \psi) - \sin\ (\alpha_{p1} - \psi)] \cdot \exp\ \{(-wt - \alpha_{p1})\ \cot\ \psi\} \div [1 - \exp\ (-\pi\ \cot\ \psi)]] - E_{bn}. \tag{5}$$

The instants at which i_{an} becomes minimum and maximum can be obtained by solving the expression for current slope. Since there are two expressions representing the armature current in different intervals, it is useful to identify the interval in which i_{an} becomes minimum or maximum. The instant at which it becomes minimum depends upon which of the discontinuous current modes comes in contact with the continuous current mode at the critical point (i.e., when the current is just continuous). This information is provided in Fig. 3, describing the interrelationship between the various modes of operation. Thus in the case of mode 4, $\alpha_{p1} \leqslant X < \pi$. The maximum of i_{an} always occurs at an angle larger than α_{p1}. Therefore, it is enough if the expression for current slope is obtained in the interval $\alpha_{p1} < wt < \pi$, by differentiating (5).

Mode 10: For the interval $0 < wt < \alpha_{p2}$,

$$i_{an} = 0.5\ \cos\ \psi[\sin\ (wt - \psi) + [3\ \sin\ \psi - \sin\ (\alpha_{p2} - \psi)\ \exp\ \{-(\pi - \alpha_{p2})\ \cot\ \psi\}]\ \exp\ (-wt\ \cot\ \psi) \div [1 - \exp\ (-\pi\ \cot\ \psi)]] - E_{bn} \tag{6}$$

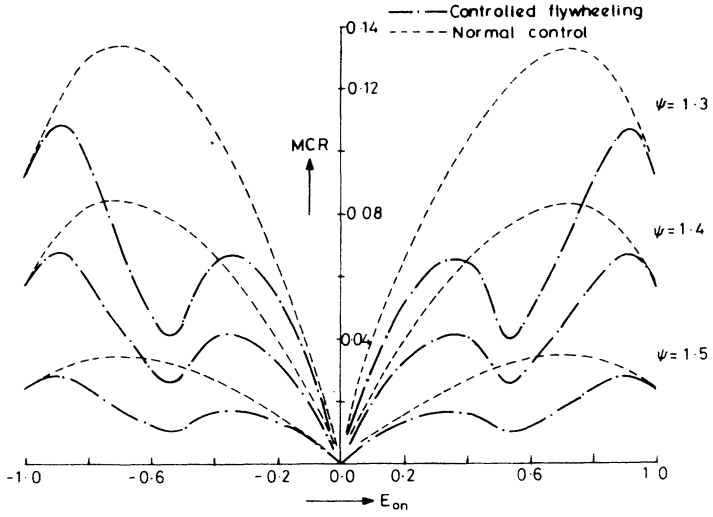

Fig. 6. Normalized maximum armature current ripple.

and for the interval $\alpha_{p2} < wt < \pi$,

$$i_{an} = 0.5 \cos \psi[2 \sin (wt-\psi) + [3 \sin \psi \exp (-\alpha_{p2} \cot \psi) - \sin (\alpha_{p2}-\psi)] \cdot \exp \{-(wt-\alpha_{p2}) \cot \psi\} \div [1-\exp (-\pi \cot \psi)]] - E_{bn}. \quad (7)$$

From Fig. 3(b), it can be seen that at the critical point, X can be on either side of α_{p2}. Therefore, expressions for current slope for the entire half-cycle have to be derived by differentiating (6) and (7). Note that more than one local maximum and minimum can exist (as in the case of mode 10 meeting mode 9), of which the absolute maximum and minimum have to be selected for the calculation of MCR.

Mode 13: For the interval $0 < wt < \alpha_{n1}$,

$$i_{an} = -0.5 \cos \psi[\sin (wt-\psi) + [\sin \psi + \sin (\alpha_{n1}-\psi) \exp \{-(\pi-\alpha_{n1}) \cot \psi\}] \cdot \exp (-wt \cot \psi) \div [1-\exp (-\pi \cot \psi)]] - E_{bn}, \quad (8)$$

and for the interval $\alpha_{n1} < wt < \pi$,

$$i_{an} = -0.5 \cos \psi[\sin \psi \exp (-\alpha_{n1} \cot \psi) + \sin (\alpha_{n1}-\psi)] \exp \{-(wt-\alpha_{n1}) \cot \psi\} \div [1-\exp (-\pi \cot \psi)]] - E_{bn}. \quad (9)$$

In this case, Y will always be smaller than $(\pi - \gamma_{n1})$, and from Fig. 3(c) it can be seen that $X \leqslant \alpha_{n1}$. Therefore, the expression for current slope in the interval $0 < wt < \alpha_{n1}$ is obtained by differentiating (8).

Mode 19: For the interval $0 < wt < \alpha_{n2}$,

$$i_{an} = -0.5 \cos \psi[2 \sin (wt-\psi) + [3 \sin \psi + \sin (\alpha_{n2}-\psi) \exp \{-(\pi-\alpha_{n2}) \cot \psi\}] \cdot \exp (-wt \cot \psi) \div [1-\exp (-\pi \cot \psi)]] - E_{bn}, \quad (10)$$

and for the interval $\alpha_{n2} < wt < \pi$

$$i_{an} = -0.5 \cos \psi[\sin (wt-\psi) + 3 \sin \psi \exp (-\alpha_{n2} \cot \psi) + \sin (\alpha_{n2}-\psi)] \cdot \exp \{-(wt-\alpha_{n2}) \cot \psi\} \div [1-\exp (-\pi \cot \psi)]] - E_{bn}. \quad (11)$$

In this case, X can be on either side of α_{n2} (Fig. 3(d)). Therefore, the expressions for current slope are obtained by differentiating (10) and (11).

Fig. 6 shows the plot of MCR for the entire range of output voltage variation for both controlled flywheeling and normal control techniques. The peak of MCR curve occurs at different output voltages for the two control techniques. The plot of the peak values of MCR against armature circuit time constant is given in Fig. 7.

B. Separation of Continuous and Discontinuous Armature Current Zones

Having obtained the value of X in the previous section, the value of critical motor back EMF E_{bnc}, at which the armature current is just continuous, can be obtained by forcing $i_{an}(X) = 0$ in (5), (6) and (7), (8), and (10) and (11) of modes 4, 10, 13, and 19, respectively. Since the armature current is continuous, its average value is directly proportional to the difference between the average converter output voltage and the motor back EMF. Therefore, normalized critical values of current I_{anc} for these modes of operation will be as follows:

$$\text{mode 4: } I_{anc} = \frac{1}{4}(1+\cos \alpha_{p1}) - E_{bnc} \quad (12a)$$

$$\text{mode 10: } I_{anc} = \frac{1}{4}(3+\cos \alpha_{p2}) - E_{bnc} \quad (12b)$$

$$\text{mode 13: } I_{anc} = \frac{1}{4}(\cos \alpha_{n1} - 1) - E_{bnc} \quad (12c)$$

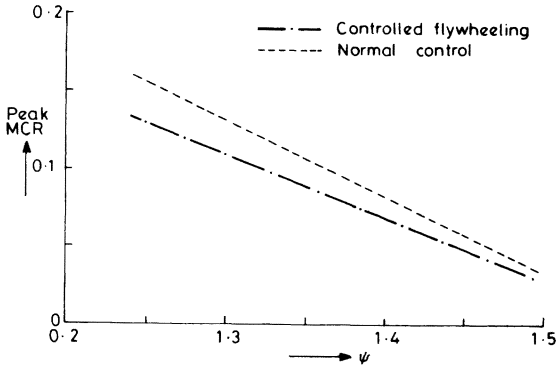

Fig. 7. Normalized peak MCR versus armature circuit time constant.

$$\text{mode 19: } I_{anc}=\frac{1}{4}(\cos\ \alpha_{n2}-3)-E_{bnc}. \qquad (12d)$$

Fig. 8 shows the normalized boundary curves separating the regions of continuous and discontinuous armature conduction for both controlled flywheeling and normal control techniques. The armature current is continuous to the right of the boundary curve.

With the help of these boundary curves and MCR characteristics, a filter inductance can be chosen such that the armature current remains continuous and the current ripple is kept within the permissible limits for worst-case load conditions. From the knowledge of load on the motor shaft, a normalized contour of minimum torque for the whole range of motor speed is obtained and superposed over the boundary curves of Fig. 8. A filter inductance is chosen so that the boundary curve corresponding to the modified armature circuit time constant falls to the left of the minimum load contour. The value of filter inductance required to keep the MCR within the specified permissible limit (usually prescribed by the manufacturers of the motor) is obtained from Fig. 7. The higher of the two values is finally chosen as the optimum filter inductance. Since the curves of Figs. 6 and 7 are drawn for normalized variables, they can be used for any dc motor. In the case of controlled flywheeling, a smaller value of filter inductance is needed to eliminate discontinuous conduction and to keep the ripple within permissible values.

IV. Analysis

A normalized equation of the system is given in (2). The system is analyzed by simulating it in a digital computer, taking into account all the modes of converter operation. For any particular choice of firing angle and motor back EMF, the waveforms of converter output voltage, armature current, and source current are obtained, from which the various parameters of system performance are calculated. The performance characteristics include motor speed–torque characteristics, armature current ripple, system efficiency, overall power factor, source current distortion factor, source current harmonics, and rms value of source current. A computer flowchart indicating the various steps of analysis is shown in Fig. 5(b).

The formulas used for the calculation of system parameters

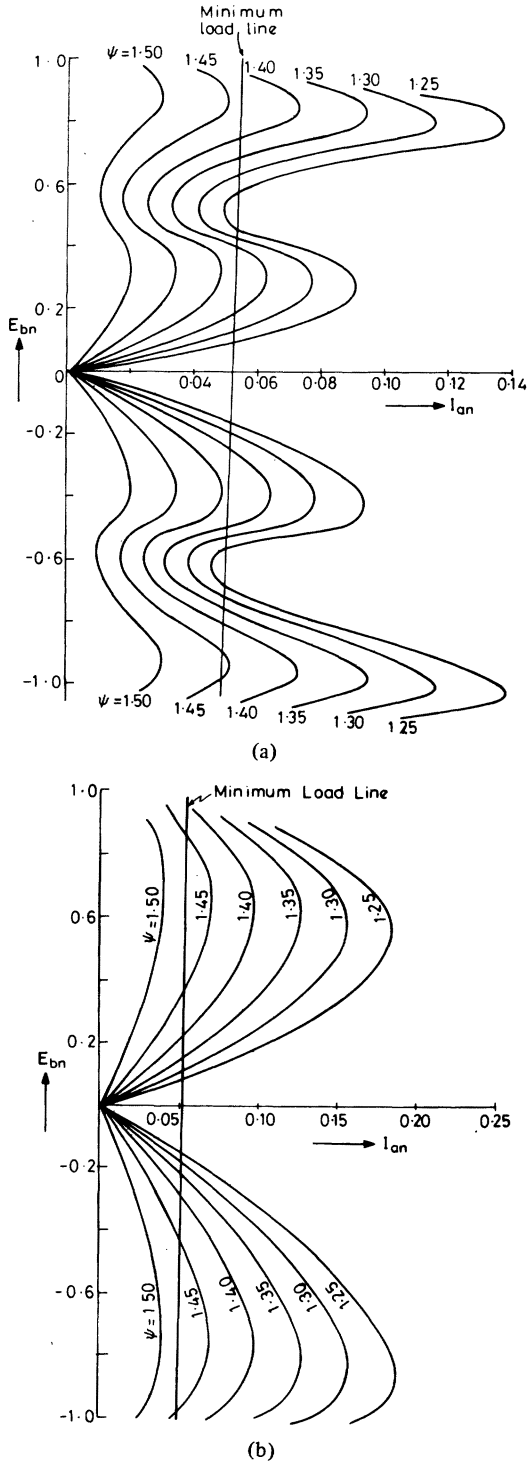

Fig. 8. Boundary curves separating regions of continuous and discontinuous armature conduction. (a) Controlled flywheeling. (b) Normal control.

are

$$\text{armature current ripple}=\text{CR}=\frac{i_{an\max}-i_{an\min}}{2} \qquad (13)$$

$$\text{overall power factor}=\text{PF}=\frac{\frac{1}{\pi}\int_0^{\pi} e_n i_{an}\ dwt}{\frac{\pi}{2\sqrt{2}} I_{sn}} \qquad (14)$$

source current distortion factor = DF

$$= \frac{\text{fundamental component of source current } I_{1n}}{\text{rms value of source current } I_{sn}}. \quad (15)$$

The efficiency of the system is defined separately for motoring and regeneration conditions:

$$\text{motoring efficiency} = \eta_M = \frac{\text{power developed by the motor}}{\text{input power to the system}}$$

$$= \frac{E_{bn} I_{an}}{\frac{1}{\pi}\int_0^{\pi} e_n i_{an}\, dwt} \quad (16)$$

regeneration efficiency

$$= \eta_R = \frac{\text{power delivered to the source}}{\text{power generated by the motor}}$$

$$= \frac{\frac{1}{\pi}\int_0^{\pi} e_n i_{an}\, dwt}{E_{bn} I_{an}}. \quad (17)$$

The system performance is investigated on a 2.2-kW dc motor (Table III) load. Normalized speed–torque characteristics are obtained by plotting E_{bn} against I_{an} (Fig. 9). Since the range of firing angle for controlled flywheeling and normal control are different, the speed–torque characteristics are drawn for constant values of E_{on}. All the other system parameters such as armature current ripple, system efficiency, overall power factor, source current distortion factor, and third harmonic in source current are plotted against I_{an} for constant values of E_{bn}, in Figs. 9–14. The fact that E_{bn} is held constant in plotting these curves facilitates the comparison of the two control techniques for the same developed power.

V. Drive Performance and Experimental Verification

The motor speed–torque characteristics and system efficiency are verified experimentally for the technique of controlled flywheeling. The experimental results are indicated by (o) in the corresponding diagrams. From the system performance characteristics, the following important points are noted.

1) Controlled flywheeling causes considerable improvement in the linearity of the motor speed–torque characteristics (Fig. 9). This is attributed to the reduction in the zone of discontinuous armature conduction.

2) The armature current ripple for controlled flywheeling is smaller than that of normal control techniques (Fig. 10), which results in higher system efficiency (Fig. 11), better machine commutation and lower derating of the motor.

3) A notable improvement in power factor occurs, especially at medium speed of the motor (Fig. 12). At the same time, however, the source current distortion factor reduces with controlled flywheeling (Fig. 13), indicating an increase in the percentage of source current harmonics. The increase in the harmonic content is attributed to the abrupt discontinuity in the source current caused by the flywheeling of the load. The

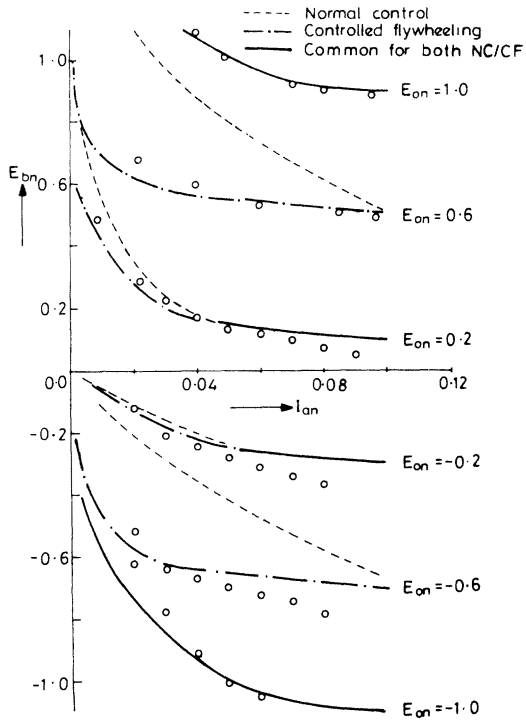

Fig. 9. Motor speed–torque characteristics.

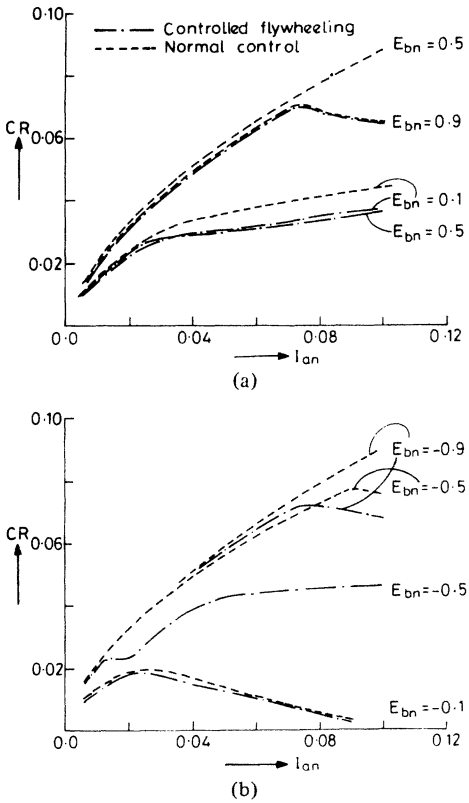

Fig. 10. Normalized armature current ripple. (a) Motoring. (b) Regenerating.

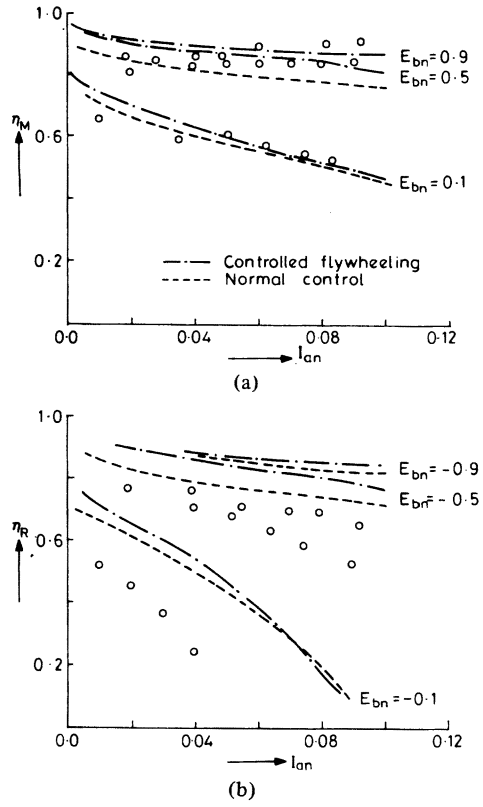

Fig. 11. System efficiency. (a) Motoring. (b) Regenerating.

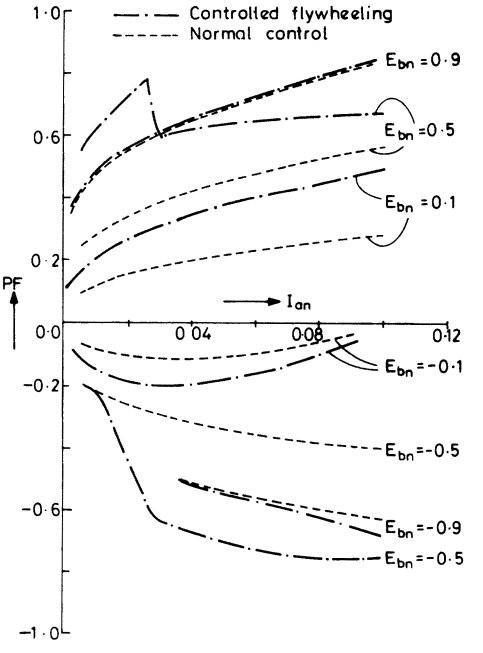

Fig. 12. Overall system power factor.

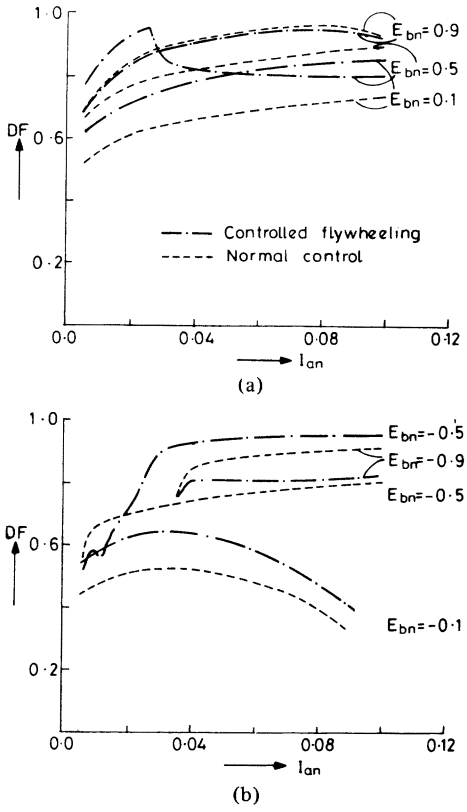

Fig. 13. Source current distortion factor. (a) Motoring. (b) Regenerating.

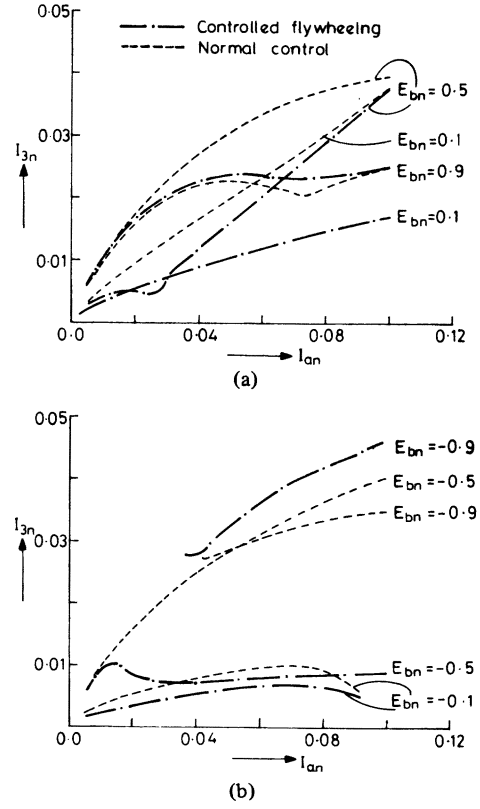

Fig. 14. Third harmonic component in source current. (a) Motoring. (b) Regenerating.

important harmonics (3, 4, 7, 9, and 11) were also calculated. The increase in magnitude of harmonics was mainly in the higher frequency range; low-frequency harmonics were in fact reduced, particularly at low speeds. As an example the third harmonic is plotted in Fig. 14.

4) The experimental results corroborate reasonably well with the theoretical characteristics in the first quadrant, but register a deviation in the fourth quadrant (Figs. 9 and 11). The discrepancy is attributed mainly to the demagnetizing effect of the armature reaction but partly to the device and brush contact resistances. The effect of armature reaction is to make the actual magnitude of motor speed larger than the predicted value in both the quadrants. However, the device and brush contact resistances tend to make the actual speed smaller than the predicted value in the first quadrant and larger in the fourth. Thus the effects of both armature reaction and brush resistance weigh together in the fourth quadrant, causing notable deviation between the theoretical and experimental results. However, in the first quadrant, these effects tend to cancel each other.

VI. Conclusion

The various modes of converter operation are identified, and their oscillograms are presented. The digital simulation approach adopted in the present case takes into account all the modes of converter operation and provides a complete analysis of the system including armature current ripple, system efficiency, power factor, source current harmonics, etc.

An analytical approach is presented to obtain normalized nomograms for maximum armature current ripple and boundary curves separating the regions of continuous and discontinuous armature conduction in the speed–torque plane. With the help of these nomograms an optimum value of filter inductance can be chosen for any dc motor.

As compared to normal control, the controlled flywheeling technique offers the advantages of higher power factor, higher system efficiency, and lower load current ripple. The disadvantages of controlled flywheeling are the increase in the source current harmonics and the complexity of control circuit. Controlled flywheeling causes significant reduction in the MCR and the region of discontinuous conduction. As a result, the optimum value of filter inductance is also considerably reduced for the controlled flywheeling technique. Since the two-stage converter with controlled flywheeling offers the same system performance as that of four-stage fully controlled converter with conventional control, this technique will find wide use in traction applications.

Nomenclature

e, E_o	Instantaneous and average output voltage of converter, V.
E_b	Motor back EMF, V.
E_m	Peak value of supply voltage, V.
e_n, E_{on}, E_{bn}	Normalized values of e, E_o, and E_b.
i_a, I_a	Instantaneous and average armature current, A.
i_{an}, I_{an}	Normalized values of i_a and I_a.
X	Angle at which i_a is a minimum, rad.
Y	Angle at which i_a is a maximum, rad.
MCR	Normalized maximum armature current ripple.
α_{p1}, α_{p2}	Converter firing angles, rad.
α_{n1}, α_{n2}	Converter flywheeling angles, rad.
β_{p1}, β_{p2}, β_{n1}, β_{n2}	Extinction angles, rad.
γ_{p1}	$=\sin^{-1}(2E_b/E_m)$, rad.
γ_{p2}	$=\sin^{-1}(E_b/E_m)$, rad.
γ_{n1}	$=\pi + \sin^{-1}(2E_b/E_m)$, rad.
γ_{n2}	$=\pi + \sin^{-1}(E_b/E_m)$, rad.
ψ	$=\tan^{-1}(\omega L_a/R_a)$, rad.
w	Supply frequency, rad/s.

References

[1] P. C. Sen, *Thyristor DC Drives.* New York: Wiley, 1981.

[2] W. Farrer and D. F. Andrew, "Fully controlled regenerative bridges with half controlled characteristics," *Proc. Inst. Elec. Eng.*, vol. 125, pp. 109–122, Feb. 1978.

[3] W. Drury, W. Farrer, and B. L. Jones, "Performance of thyristor bridge converters employing flywheeling," *Proc. Inst. Elec. Eng.*, pt. B, *Elec. Power Appl.* vol. 127, pp. 268–276, July 1980.

[4] H. K. Patel and G. K. Dubey, "Modified sequence control technique for improving the performance of regenerative bridge converters," *IEEE Trans. Ind. Appl.*, vol. IA-19, pp. 682–689, Nov./Dec. 1982.

[5] G. K. Dubey, "Calculation of filter inductance for chopper fed dc separately excited motor," *Proc. IEEE,* vol. 66, pp. 1671–1673, Dec. 1978.

Subbanna P. Bhat, for a photograph and biography please see page 1440 of this issue.

Gopal K. Dubey (SM'83), for a photograph and biography please see page 1440 of this issue.